Mechatronics 118 (2026) 103534

Contents lists available at ScienceDirect

Mechatronics

journal homepage: www.elsevier.com/locate/mechatronics

Adaptive gripper fingers with passively aligning articulated hemispherical pads☆

Tilen Klemenčič, Marko Munih, Matjaž Mihelj *, Janez Podobnik

University of Ljubljana, Faculty of Electrical Engineering, Tržaška cesta 25, Ljubljana, 1000, Slovenia

ARTICLE INFO

Keywords:
Grippers
Grasping
Compliant mechanism
Adaptive gripper finger
Robotic manipulation

ABSTRACT

Robotic grippers require both adaptability to diverse object shapes and sufficient strength for robust manipulation. This study presents adaptive gripper fingers that combine passively aligning articulated hemispherical pads with a compliant silicone layer to improve shape accommodation and force transmission during grasping. The structure features hemispherical pads embedded in low-friction grooves, allowing passive alignment to local object geometry during contact. A low-cost fabrication process involving 3D printing and silicone molding is employed, making the design suitable for various applications. Experimental validation was conducted using pull-off force tests on multiple 3D-printed objects selected to represent a range of characteristic object geometries, along with deformation measurements on a soft object. Results show that, for the tested objects and grasping conditions, the proposed design improves pull-off performance and reduces deformation of a soft test object relative to the evaluated reference finger designs.

1. Introduction

Robotic grippers are vital to modern automation, enabling the manipulation of objects with varying shapes, sizes, and surface properties [1]. For reliable grasping, robotic grippers must optimally apply grasp forces to prevent slippage or damage while accommodating diverse object shapes and material properties [2]. Conventional rigid grippers can generate high forces but require precise positioning and fail to conform to geometric variability, whereas soft grippers readily adapt to object shape but suffer from limited load-bearing capacity and poor force transmission under higher loads [2,3]. This fundamental trade-off between geometric adaptability and grasp strength is restricting potential applications, especially in tasks demanding both delicate interaction and high-force manipulation [3–5].

Recent advancements in adaptive gripper technology have produced three primary design approaches: soft fingers [6–8], underactuated fingers [9,10], and compliant fingers [11]. Soft fingers achieve excellent shape conformity but rely on material deformation for force transmission, which limits their performance under high loads [7,12]. Underactuated fingers can generate larger forces through mechanical coupling, yet their contact geometry remains largely fixed once engaged, restricting adaptability to complex object shapes [9,10]. Compliant and hybrid designs attempt to balance these properties, including recent approaches based on topology optimization that tailor stiffness distributions to improve force transmission and structural efficiency [13,14]. These designs typically achieve adaptability through elastic deformation rather than by reorienting load-bearing contact elements, resulting in limited improvement in grasp stability under directional disturbances [15,16].

In this work, we present an adaptive gripper finger design that combines passively aligning rigid contact elements with a compliant surface layer to improve both geometric accommodation and load transmission during grasping. The design uses multiple articulated hemispherical pads embedded in low-friction grooves, allowing passive reorientation of local contact normals as the fingers conform to the object. The work focuses on the mechanical integration of these elements and on experimentally evaluating their effect on pull-off performance and soft-object deformation.

The main contributions of this work are:

- An adaptive gripper finger architecture that combines passively aligning articulated hemispherical pads with a compliant silicone layer.
- A supporting grasp analysis used to interpret how passive pad reorientation influences contact orientation, grasp wrench space, and pulling-force capacity in the tested configurations.
- An analytical pulling-force model linking grasp force, friction, and contact orientation.

☆ This paper was recommended for publication by Associate Editor Oliver Sawodny.

* Corresponding author.
E-mail address: matjaz.mihelj@fe.uni-lj.si (M. Mihelj).

https://doi.org/10.1016/j.mechatronics.2026.103534
Received 25 February 2026; Received in revised form 2 April 2026; Accepted 21 April 2026
Available online 28 April 2026

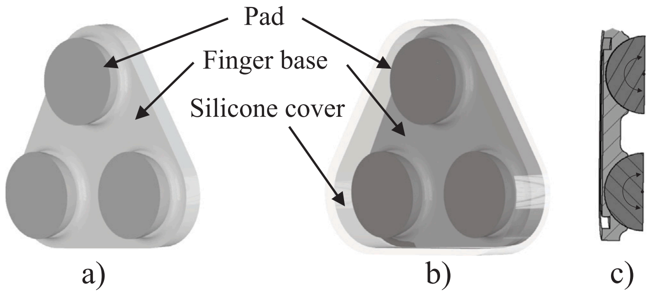

Fig. 1. (a) Adaptive gripper finger with three passively aligning articulated hemispherical pads. (b) Same finger configuration with an added soft silicone cover encapsulating all three pads. (c) Cross-sectional side view illustrating the passive rotation of the hemispherical pads.

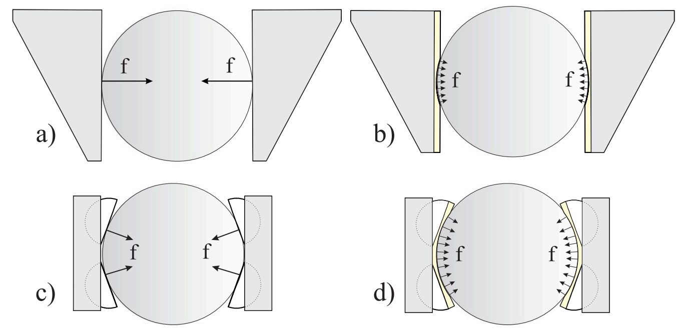

Fig. 2. Force distribution applied to a spherical object by finger types: (a) flat fingers, (b) flat fingers with a soft layer, (c) adaptive fingers, (d) adaptive fingers with a soft layer.

- A comparative experimental evaluation against flat, soft-layer, and Fin Ray finger designs using pull-off force tests and soft-object deformation measurements.

The proposed adaptive finger design is evaluated through three complementary experimental studies. First, systematic pull-off force experiments [17–19] are conducted across multiple object geometries to quantify pull-off performance and force transmission. Second, a comparative analysis of force-controlled and position-controlled grasping is performed to illustrate the force-closure and form-closure regimes in the tested setup. Third, deformation experiments on an instrumented soft object are carried out to assess the ability of the proposed fingers to reduce object deformation during grasping. The contribution of this work lies primarily in the mechanical design and experimental validation of the finger architecture, while the analytical models are used to interpret the observed grasping behavior. Together, these experiments show improved pull-off performance and reduced soft-object deformation relative to the tested reference finger designs.

2. Methods

2.1. Adaptive fingers concept

The objective of this work is to design robotic gripper fingers that can adapt to representative object geometries while achieving high pulling forces at low grasp forces. This requirement is particularly important when handling soft, deformable, or fragile objects, where excessive normal force can cause damage, but it is equally relevant for applications demanding robust force transmission. Preliminary evaluations of conventional soft finger designs revealed insufficient structural stiffness under load, motivating the development of a rigid yet adaptive finger architecture that preserves shape conformity while maintaining high load-bearing capacity.

To address this limitation, we developed an adaptive contact surface composed of multiple passively aligning articulated hemispherical pads. Each pad is mounted in a low-friction groove that allows free rotation about its center, enabling the contact surface to passively conform to local object geometry during grasping. In the proposed design, each finger includes three hemispherical pads arranged in an equilateral triangle configuration (illustrated in Fig. 1), which was found to offer the most versatile performance across the representative object geometries considered in this study. However, the pad layout is not limited to this arrangement; different numbers and configurations of pads can be implemented depending on application requirements. The independent rotation of each pad ensures consistent surface contact and pressure distribution, even on uneven or complex object geometries.

When manipulating soft or fragile objects, maximizing the contact area is essential to reduce localized pressure and minimize the risk of damage. A larger contact surface allows the applied forces to be distributed more evenly across the object. As shown in Fig. 2, passively aligning pads increase the number of contact points from two to four relative to conventional straight fingers. Adding a soft layer to straight fingers further increases the contact area, transforming point contacts into small surface contacts, depending on the material properties and layer thickness. Combining passively aligning pads with a soft layer significantly enhances the overall contact area. The pads passively conform to the object's shape, while the soft layer adds compliance and cushioning. These four finger configurations, flat fingers, flat fingers with a soft layer, adaptive fingers and adaptive fingers with a soft layer, are illustrated in Fig. 2, highlighting the differences in contact areas.

To optimize the pad and groove geometry, we evaluated three spherical segments (hemispherical, sub-hemispherical, or super-hemispherical) to maximize torque about the sphere's center. Using torque equations we analyze the hemispherical pad first. As shown in Fig. 3(a), a force f applied at angle β to the pad's straight edge produces torque τ, with moment arm r, expressed as:

$$\tau = r f \sin\beta. \tag{1}$$

With β ranging from 0° to 180°, τ remains positive, producing counterclockwise rotation about the pad's center.

For sub-hemispherical or super-hemispherical pads, shown in Figs. 3(b) and 3(c), the moment arm changes to $r' = \sqrt{r^2 + h^2}$, where h is the perpendicular distance from the center. The angle between r' and f is $\Phi + 90° - \beta$, yielding:

$$\tau = \sqrt{r^2 + h^2} f \cos(\Phi - \beta). \tag{2}$$

Torque τ is positive (aligned with the direction of the applied force) when $\Phi - \beta$ lies between −90° and 90°. Outside this range, τ reverses direction, reversing the pad's rotation and risking unstable grasping that could dislodge the object. Given that β is constrained between 0° and +180°, setting $\Phi = 90°$ ensures that τ always acts in the positive direction.

Each pad shape yields distinct torque characteristics. For a hemispherical pad, maximum torque occurs at $\beta = 90°$, typical at initial contact, ensuring optimal grasp stability. Other shapes achieve peak torque at varying angles β. This is less consistent for general grasping but could prove useful for specific applications. Thus, we selected hemispherical pads for their versatility across most scenarios.

2.2. Grasp closure analysis

Achieving a stable grasp in robotic manipulation relies on two fundamental concepts: form closure and force closure. Form closure occurs when an object is fully constrained by the geometric arrangement of the contacts, such that no motion is possible without interpenetrating a contact surface. This condition is purely kinematic and does not require friction [20]. In contrast, force closure requires that the contact

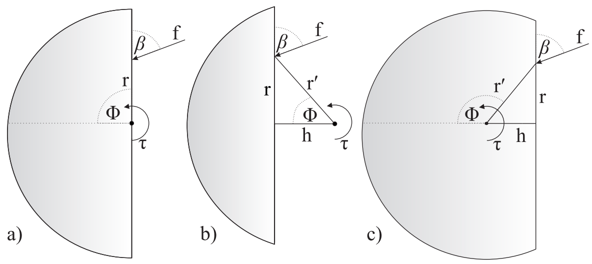

Fig. 3. Illustrations of three distinct pad geometries: (a) hemispherical, (b) sub-hemispherical, (c) super-hemispherical. In each case, an external force f is applied at an angle β relative to the surface of the pad.

forces, subject to friction constraints, can resist any externally applied wrench [21]. Unlike form closure, force closure allows nonzero relative motion at contacts, provided that friction compensates for external disturbances. Force closure enables controlled interaction by modulating contact forces within the friction cone limits and is often more appropriate for manipulation tasks requiring precise force regulation. The proposed gripper design supports both modes depending on the gripper's control strategy. Under position control, the articulated pads conform geometrically to the object, potentially achieving form closure through kinematic constraint. Under force control, the pads rotate to align their contact normals with the object surface, maximizing frictional support and enabling robust force closure. The following analysis formalizes these concepts first in planar settings and later extends them to three-dimensional grasps.

2.2.1. Planar grasp modeling

For simplicity, we first consider the planar case, commonly used in theoretical grasp planning analyses [16,21]. In a planar grasp with k contact points, the admissible contact forces generate wrenches spanning the 2D planar wrench space. The grasp matrix $\mathbf{G}$ maps the contact force vector $\mathbf{f} = [\mathbf{f}_1^T, \dots, \mathbf{f}_k^T]^T$ (where each $\mathbf{f}_i$ acts at $\mathbf{r}_i = [x_i, y_i]^T$) to the net wrench $\mathbf{w} = [f_x, f_y, \tau]^T$:

$$\mathbf{w} = \mathbf{G}\mathbf{f},$$

$$\mathbf{G} = \begin{bmatrix} \mathbf{G}_1 & \mathbf{G}_2 & \cdots & \mathbf{G}_k \end{bmatrix}, \quad \mathbf{G}_i = \begin{bmatrix} 1 & 0 \\ 0 & 1 \\ -y_i & x_i \end{bmatrix} \tag{3}$$

The net wrench includes the net force and torque acting on the object.

Each contact force is modeled using the hard-finger assumption[1] with Coulomb friction:

$$\mathbf{f}_i = f_{n,i}\mathbf{n}_i + f_{t,i}\mathbf{t}_i, \qquad |f_{t,i}| \le \mu f_{n,i}, \quad f_{n,i} \ge 0,$$

where $\mathbf{n}_i$ and $\mathbf{t}_i$ are the normal and tangential unit directions at contact i. This defines the planar friction cone

$$\mathcal{F}_i = \left\{ \mathbf{f}_i = f_{n,i}\mathbf{n}_i + f_{t,i}\mathbf{t}_i \,:\, f_{n,i} \ge 0,\, |f_{t,i}| \le \mu f_{n,i} \right\},$$

with half-angle $\alpha = \arctan(\mu)$.

To characterize the wrenches that can be generated from normal forces alone, we construct the wrench matrix

$$\mathbf{W} = \begin{bmatrix} \mathbf{n}_1 & \mathbf{n}_2 & \cdots & \mathbf{n}_k \\ \mathbf{r}_1 \times \mathbf{n}_1 & \mathbf{r}_2 \times \mathbf{n}_2 & \cdots & \mathbf{r}_k \times \mathbf{n}_k \end{bmatrix}.$$

Each column is a primitive wrench $\mathbf{w}_i$.

Form closure requires:

[1] In planar settings, hard-finger and soft-finger models are equivalent because there is no rotational degree of freedom about the surface normal.

1. $\mathbf{W}$ has full row rank (3 in planar case, 6 in 3D), 2. the number of frictionless contacts satisfies the minimum closure condition (4 in planar case, 7 in 3D), 3. there exists $\lambda > \mathbf{0}$ such that

$$\mathbf{W}\lambda = \mathbf{0}.$$

This ensures that the origin lies strictly inside the convex hull of the grasp wrench space.

For frictional contacts, each contact contributes two primitive wrenches corresponding to the edges of the friction cone [22]:

$$\mathbf{w}_i^+ = \begin{bmatrix} \mathbf{n}_i + \mu\mathbf{t}_i \\ \mathbf{r}_i \times (\mathbf{n}_i + \mu\mathbf{t}_i) \end{bmatrix}, \qquad \mathbf{w}_i^- = \begin{bmatrix} \mathbf{n}_i - \mu\mathbf{t}_i \\ \mathbf{r}_i \times (\mathbf{n}_i - \mu\mathbf{t}_i) \end{bmatrix}.$$

Collecting all friction edges gives the full planar wrench matrix:

$$\mathbf{W} = \left[\mathbf{w}_1^+, \mathbf{w}_1^-, \dots, \mathbf{w}_k^+, \mathbf{w}_k^-\right].$$

Force closure is achieved if the matrix $\mathbf{W}$ has full row rank and the origin lies strictly within the convex hull of the grasp wrench space (GWS), which is defined by the union of the friction cones [21]. These forces must satisfy both equilibrium and friction constraints. Formally, the grasp can resist any external wrench $\mathbf{w}_{\text{ext}}$ if there exists a vector of contact forces $\mathbf{f}$, such that:

$$\mathbf{G}\mathbf{f} = -\mathbf{w}_{\text{ext}}. \tag{4}$$

Force closure generalizes form closure by incorporating frictional constraints to resist external wrenches. Where form closure requires strict geometric immobilization (4 contacts in 2D and 7 contacts in 3D), force closure achieves stability through friction with significantly fewer contacts: two hard finger contacts in 2D or two soft finger contacts in 3D [20].

For a circular object of radius rr, with the coordinate frame attached to the object center, parameterized by contact angles θ_i, the friction-cone edge wrenches become

$$\mathbf{w}_i^{\pm} = \begin{bmatrix} -\cos(\theta_i \pm \alpha) \\ -\sin(\theta_i \pm \alpha) \\ \mp r \sin\alpha \end{bmatrix}. \tag{5}$$

We observe that if the contact is frictionless ($\sin\alpha = 0$), the rank of matrix $\mathbf{W}$ reduces to 2 because the last row consists entirely of zeros. This means that form closure on a round object without friction cannot be achieved, since the object can freely rotate in the fingers. However, we can evaluate partial form closure for translational motion by removing the last row of $\mathbf{W}$, resulting in a matrix of dimension $2\times2k$. For partial form closure (resisting all translational disturbances), the convex cone of $\mathbf{W}$ must span $\mathbb{R}^2$, the reduced $\mathbf{W}$ has full row rank of 2, and the origin must lie in the interior of the convex cone of $\mathbf{W}$. A grasp satisfying these conditions ensures resistance to arbitrary translational disturbances. This is represented by blue rectangular convex hull shown in Fig. 4(a). We can also construct the wrench matrix $\mathbf{W}$ for parallel fingers by setting $\theta_1 = 0°$ and $\theta_2 = 180°$ in Eq. (5). The resulting matrix $\mathbf{W}$ has rank 1. This indicates that the grasp can only resist disturbances along the axis connecting the contacts (compression), offering no resistance to translation perpendicular to the grasp axis or rotation without friction.

In case of a contact with friction ($\alpha \neq 0$) in planar example, the rank of wrench matrix $\mathbf{W}$ is 3 and force closure can also constrain rotational movement of the object. In the proposed adaptive fingers, the articulated pads rotate to align with the local object surface. This adaptive design allows each pad to conform to the object's surface, creating multiple contact points that may establish form closure. In case of force closure, the rotation of pads enhances the effective coverage of the friction cones. Additionally, the soft silicone layer increases surface friction, allowing stable grasps to be achieved with reduced normal force magnitudes. These effects are further validated by the experimental results presented in Section 3.

To visualize the grasp wrench space for a spherical object in the planar case, we focus on normal and friction cone force components.

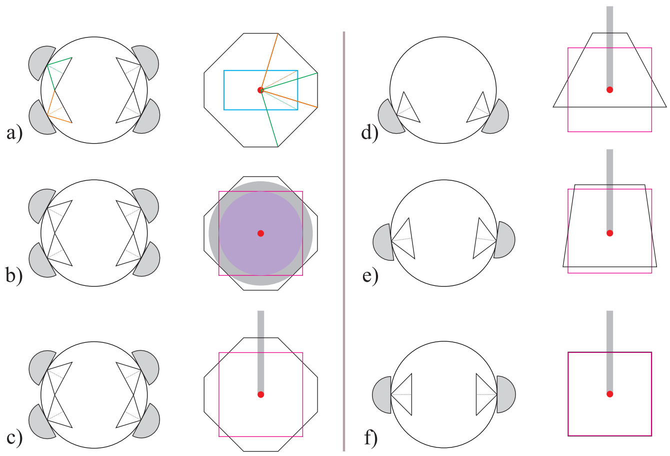

Fig. 4. Force closure phases for a spherical object grasped by an adaptive fingers (left), visualized through grasp wrench spaces (GWS, right) for adaptive (black) and flat parallel (magenta) fingers. Figs show: force closure GWS (black) versus form closure GWS (blue); (b) initial four-cone GWS (black) versus two-cone GWS (magenta); (c-f) evolving GWS under a downward pulling force, with task wrench space (gray vertical line, $-\mathbf{w}_{\text{ext}}$). The adaptive fingers GWS exceeds the flat parallel fingers until (f), equalizes at parallel pad alignment.

The GWS is then represented as the convex hull of normals of contact forces (in case of form closure) or as the convex hull of contact forces within the friction cones (in case of force closure). As shown in Fig. 4, inclusion of the origin in convex hull indicates the ability to resist translational disturbances, a key aspect of grasp stability. Fig. 4(a) shows GWS hulls for adaptive finger for form closure as a blue convex hull, black convex hull for force closure where all four pads are in contact with the object, with the grasp wrench space spanning the origin (red circle). Fig. 4(a) additionally illustrates the construction of the GWS convex hull. The right-side friction cones and their corresponding normals are color-coded (green and orange). Contact normals, represented by dashed lines, are used to construct the form closure GWS (blue convex hull). Similarly, solid lines depicting the friction cone edges are used to generate the force closure GWS convex hull. Fig. 4(b) shows GWS hull in black for adaptive fingers for force closure and magenta convex hull for force closure for parallel fingers. Fig. 4(c-f) shows four stages of force closure with adaptive fingers (black GWS hull) versus flat fingers (magenta). The left side of each subfigure shows the object with articulated pads, while the right side displays the GWS. Initially (a-c), adaptive fingers form four friction cones, resulting in a broader GWS hull. A key grasp quality metric is the radius of the largest sphere centered at the origin and fully contained within the GWS hull [23]. Fig. 4(b) shows this quality metric for force closure represented by circles: dark gray for adaptive fingers and magenta for parallel fingers. The larger radius of the adaptive fingers' circle indicates better grasp quality, demonstrating that stability is higher compared to parallel fingers.

The grasp quality metric based on the sphere assumes isotropic disturbances and does not account for task-specific requirements [23]. In our experiments, the primary disturbance is a downward pulling force, modeled as the task wrench $-\mathbf{w}_{\text{ext}}$. The corresponding task wrench space (TWS) is shown in Figs. 4(c–f) as a gray line representing $-\mathbf{w}_{\text{ext}}$. In stages (c–e), the adaptive fingers maintain a broader GWS compared to parallel fingers, indicating a higher capacity to resist external forces within the task-relevant direction. By Fig. 4(f), the articulated pads become parallel to the object surface, and the GWS of both designs converge. This analysis illustrates the role of pad reorientation in sustaining force closure under a vertical pulling wrench, which is further quantified in Section 2.3.1.

2.2.2. Extension to 3D grasp modeling

The previous analysis focused on planar grasps, where the grasp wrench space (GWS) is three-dimensional and described by the net force in the plane and the out-of-plane torque. In practice, the proposed adaptive fingers operate in full three dimensions. In this subsection we extend the grasp formulation to $\mathbb{R}^3$ and compare the 3D wrench spaces of the proposed adaptive fingers and conventional parallel fingers on a spherical object (Fig. 5).

We consider a rigid spherical object of radius r grasped by k hard finger contacts with Coulomb friction. The ith contact is located at position $\mathbf{r}_i = [x_i, y_i, z_i]^T$ with inward unit normal

$$\mathbf{n}_i = \frac{-\mathbf{r}_i}{\|\mathbf{r}_i\|}, \qquad \|\mathbf{n}_i\| = 1. \tag{6}$$

As in the planar case, we assume a hard finger model with Coulomb friction coefficient μ. The admissible contact forces at contact i form a 3D friction cone

$$\mathcal{F}_i = \left\{ \mathbf{f}_i = f_{n,i}\mathbf{n}_i + \mathbf{f}_{t,i} \ : \ f_{n,i} \geq 0, \ \|\mathbf{f}_{t,i}\| \leq \mu f_{n,i} \right\}. \tag{7}$$

where $f_{n,i}$ is the normal component and $\mathbf{f}_{t,i}$ the tangential component of the contact force.

To construct the grasp wrench space we linearize each friction cone by sampling forces along its boundary. Let $\mathbf{t}_{i,1}, \mathbf{t}_{i,2}$ be an orthonormal basis of the tangent plane at contact i, i.e., $\mathbf{t}_{i,1}^{\mathsf{T}}\mathbf{n}_i = \mathbf{t}_{i,2}^{\mathsf{T}}\mathbf{n}_i = 0$ and $\|\mathbf{t}_{i,1}\| = \|\mathbf{t}_{i,2}\| = 1$. For an angle $\gamma \in [0, 2\pi)$ we define a boundary force

$$\mathbf{f}_i(\gamma) = \mathbf{n}_i + \mu \left(\mathbf{t}_{i,1} \cos\gamma + \mathbf{t}_{i,2} \sin\gamma \right), \tag{8}$$

which lies on the surface of the friction cone $\mathcal{F}_i$ up to a positive scale factor. Each such force induces a primitive wrench

$$\mathbf{w}_i(\gamma) = \begin{bmatrix} \mathbf{f}_i(\gamma) \\ \mathbf{r}_i \times \mathbf{f}_i(\gamma) \end{bmatrix} \in \mathbb{R}^6. \tag{9}$$

By sampling γ at m evenly spaced angles $\gamma_j = 2\pi j/m$, $j = 1, \dots, m$, we obtain a finite set of primitive wrenches $\mathbf{w}_{i,j} = \mathbf{w}_i(\gamma_j)$.

Stacking all primitive wrenches across all contacts yields the 3D wrench matrix

$$W = \left[\mathbf{w}_{1,1}, \dots, \mathbf{w}_{1,m}, \mathbf{w}_{2,1}, \dots, \mathbf{w}_{k,m} \right] \in \mathbb{R}^{6\times km}. \tag{10}$$

The convex hull of the columns of W defines the 3D grasp wrench space,

$$\mathcal{W} = \operatorname{conv}\left(\{ \mathbf{w}_{i,j} \}_{i,j} \right) \subset \mathbb{R}^6, \tag{11}$$

which contains all wrenches that can be generated by the grasp when friction is fully utilized at the contacts.

For the comparison shown in Fig. 5 we focus on the force component of the wrench, i.e., on the first three rows of W. Denote

$$W_f = \left[I_{3\times3} \quad 0_{3\times3} \right] W \in \mathbb{R}^{3\times km}, \tag{12}$$

so that each column of W_f corresponds to a feasible net force direction. The convex hull

$$\mathcal{W}_f = \operatorname{conv}\left(\{ \mathbf{f}_{i,j} \}_{i,j} \right) \subset \mathbb{R}^3 \tag{13}$$

with $\mathbf{f}_{i,j}$ the force part of $\mathbf{w}_{i,j}$ describes the set of all normalized net forces for which an equilibrium wrench exists.

For a parallel two-finger gripper grasping a sphere along the $\pm x$–axis, both contacts share collinear inward normals

$$\mathbf{n}_1 = \begin{bmatrix} -1 & 0 & 0 \end{bmatrix}^{\mathsf{T}}, \qquad \mathbf{n}_2 = \begin{bmatrix} +1 & 0 & 0 \end{bmatrix}^{\mathsf{T}}, \tag{14}$$

so that the contact normals are collinear along the x–axis. Consequently, the subspace spanned by the normal forces has rank one. While the inclusion of friction allows the grasp to resist forces in the y and z directions, forming a 3D grasp wrench space (yellow region in Fig. 5), the grasp lacks geometric constraint in these axes. This heavy reliance on friction contrasts with the proposed adaptive design, where the spatial distribution of normals provides geometric support in all three translational directions.

In contrast, for the proposed adaptive finger with three pads per finger, the six contact points are distributed on the spherical surface. Let (θ_i, ϕ_i) denote the azimuth and elevation of contact i in spherical coordinates. The contact normals can then be written as

$$\mathbf{n}_i = \begin{bmatrix} \cos\theta_i \cos\phi_i \\ \sin\theta_i \cos\phi_i \\ \sin\phi_i \end{bmatrix}, \qquad i = 1, \dots, 6, \tag{15}$$

as also illustrated by the red normals in Fig. 5a. Since these normals are non-collinear and span $\mathbb{R}^3$, the corresponding force matrix W_f^{adp} has rank three and the force GWS $\mathcal{W}_f^{\text{adp}}$ forms a full three-dimensional convex body (blue region in Fig. 5b–d). The green regions in Fig. 5 highlight directions where the adaptive design provides a strictly larger set of feasible force wrenches than the parallel gripper.

This analysis indicates that, within the frictional hard-finger model considered here, a parallel jaw gripper with two opposing contacts provides a more limited translational force-wrench space in 3D than the proposed adaptive finger configuration with three pads per finger. Under the simplified contact assumptions used here, the distributed contact normals of the adaptive configuration span three translational directions, corresponding to partial form closure for translation, whereas the parallel gripper does not. The difference between the two force-wrench hulls in Fig. 5 illustrates this modeled property and complements the planar GWS analysis. In this study, it is used as a supporting explanation for the observed pull-off behavior in the tested configurations.

Fig. 5 presents a comparison of the three-dimensional grasp wrench spaces (GWS) between two configurations, modeled using the hard finger contact approach: (1) adaptive fingers employing three articulated pads, and (2) flat parallel fingers. Fig. 5(a) shows the contact points and normals (red: adaptive, blue: flat). Figs. 5(b)–(d) display the corresponding GWS from different viewpoints: blue volumes correspond to the adaptive fingers, yellow to the parallel fingers, and green regions indicate directions in which the modeled force-wrench space of the adaptive configuration exceeds that of the parallel configuration. Under the simplified contact assumptions used here, the parallel-finger configuration has rank 1 in the translational part of the wrench matrix, since the corresponding primitive wrench is $\mathbf{w}_i = [\pm 1, 0, 0, 0, 0, 0]^T$. For the proposed finger design with three pads per finger, the distributed contact normals span three translational directions in the model, corresponding to partial form closure for translation, with primitive wrench $\mathbf{w}_i = [\cos(\theta_i)\cos(\phi_i), \sin(\theta_i)\cos(\phi_i), \sin(\phi_i), 0, 0, 0]^T$, where θ_i and ϕ_i are the spherical coordinates of the contact points. In this study, this comparison is used as a geometric interpretation of the observed pull-off behavior in the tested configurations.

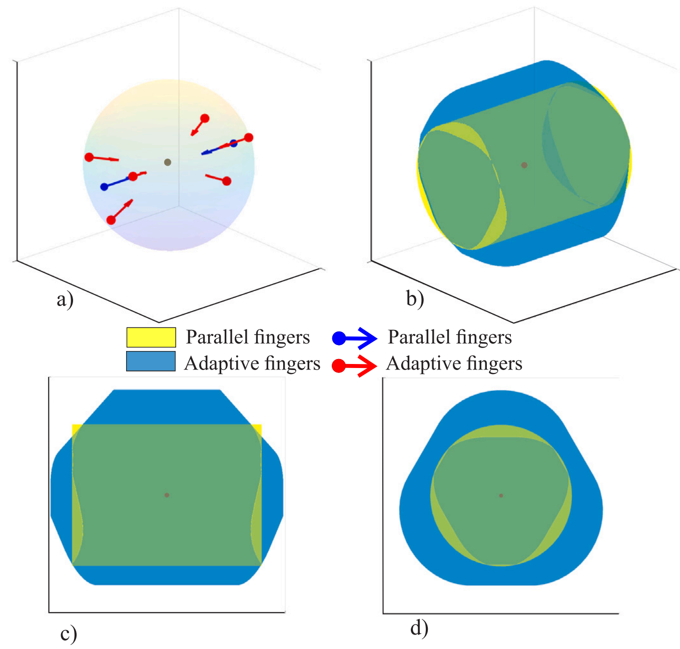

Fig. 5. Three-dimensional grasp wrench spaces (GWS) for the proposed adaptive fingers (blue volume) and flat parallel fingers (yellow volume) under the simplified hard-finger contact model used in this study. Contact points and inward normals are shown in red (adaptive) and blue (parallel). The green regions indicate directions in which the modeled force-wrench space of the adaptive configuration exceeds that of the parallel configuration. This figure illustrates how the spatial distribution of contact normals differs between the two configurations and provides a geometric interpretation of the pull-off behavior observed in the tested grasping configurations.

2.3. Pulling force analysis

2.3.1. Maximum pulling force model in 2D

To evaluate the theoretical maximum pulling force of the proposed adaptive fingers, we analyze the planar grasp configuration shown in Fig. 4(d), where two symmetric pads are in contact with a spherical object. Let f_{gr} denote the total grasp force applied by the gripper. Assuming symmetry, each pad contributes half of this force. Due to the adaptive geometry of the fingers, the pads rotate passively to align with the object's curvature, resulting in a contact normal inclined at an angle θ relative to the horizontal.

The friction cone at each contact has an angular width defined by the friction angle $\alpha = \arctan(\mu)$, where μ is the coefficient of friction between the contact surface and the object. The task is to determine the maximum pulling force f_p that the grasp can resist along the vertical axis before slippage occurs. As illustrated in Fig. 6, the extreme wrench that can be resisted corresponds to the resultant force vector lying on the upper boundary of the friction cone.

As illustrated in Fig. 4, the extreme wrench that can be resisted lies along the boundary of the combined friction cones, forming the edge of the grasp wrench space. Geometrically, the maximum pulling force corresponds to the furthest point on this boundary in the vertical direction. Fig. 6 shows the grasp wrench space with forces (f_{gr} and f_p) and angles (θ and α) indicated. Using the GWS model, we calculated the maximum pulling force as:

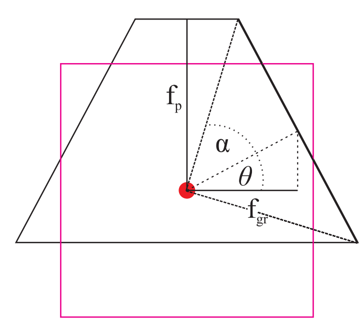

Fig. 6. Illustration of case (d) from Fig. 4, showing a spherical object grasped by two symmetric pads located at the bottom. The figure visualizes the grasp wrench space (GWS) formed by the friction cones at each contact. The grasp force f_{gr} and the pulling force f_p acting on the object are indicated.

$$f_p = \frac{f_{gr} \cdot \sin(\alpha + \theta)}{\cos(\theta) \cdot \cos(\alpha)}. \tag{16}$$

This can be algebraically simplified to:

$$f_p = f_{gr} \cdot (\tan\theta + \tan\alpha). \tag{17}$$

Since $\tan\alpha = \mu$, we can further simplify the expression as the maximum achievable pulling force:

$$f_p^{\max} = f_{gr} \cdot (\tan\theta + \mu). \tag{18}$$

This equation highlights the dual contribution to grasp stability:

1. Geometric interlocking ($\tan\theta$): As the pads rotate beneath the object ($\theta > 0°$), they create a "wedge" effect that converts horizontal grasp force into vertical resistance purely through geometry.
2. Friction (μ): The material properties provide standard frictional resistance.

When $\theta = 0°$, the pads are aligned horizontally (as in a parallel-jaw gripper), and the equation reduces to the classical friction limit $f_p = f_{gr} \cdot \mu$. Conversely, as θ increases, the term $\tan\theta$ grows, significantly amplifying the pulling force beyond what friction alone could provide. Although an idealized form closure ($\theta \to 90°$) is geometrically constrained by the object size and finger limits, this model confirms that maximizing the pad contact angle is critical for high-load manipulation.

2.3.2. Maximum pulling force model in 3D

The previous derivation was based on a planar grasp model. In the adaptive finger configuration, each finger may establish multiple non-coplanar contacts in three dimensions. The maximum pulling force is therefore determined by the intersection of the pulling direction with the boundary of the full *3D* grasp wrench space (GWS). In this section, we derive a closed-form solution, where the grasp force is defined as the total horizontal closing component of the contact forces.

Let $\mathbf{n}_i \in \mathbb{R}^3$ denote the inward unit normal at contact i, and let $\mathcal{F}_i$ denote the corresponding Coulomb friction cone with friction angle $\alpha = \arctan(\mu)$. Let $\mathbf{e}_p \in \mathbb{R}^3$ be the unit vector defining the pulling direction. Grasp equilibrium requires

$$\sum_{i=1}^{k} \mathbf{f}_i = -f_p \mathbf{e}_p, \qquad \mathbf{f}_i \in \mathcal{F}_i. \tag{19}$$

For each contact, define the inclination angle θ_i with respect to the pulling direction as

$$\sin\theta_i = \mathbf{n}_i \cdot \mathbf{e}_p. \tag{20}$$

The maximum resistive force at a contact occurs on the boundary of the friction cone. Restricting the friction force to the plane spanned by $\mathbf{n}_i$ and $\mathbf{e}_p$, the optimal contact force direction is

$$\mathbf{f}_i = f_{n,i}\left(\mathbf{n}_i \cos\alpha + \mathbf{t}_{i,p} \sin\alpha\right), \tag{21}$$

where $\mathbf{t}_{i,p}$ is the unit tangent vector within that plane opposing slip. The grasp force is defined as the sum of horizontal closing components along the (inward) finger closing directions $\mathbf{e}_{gr,i}$:

$$f_{gr} = \sum_{i=1}^{k} f_{gr,i}, \qquad f_{gr,i} = \mathbf{f}_i \cdot \mathbf{e}_{gr,i}, \qquad f_{gr,i} \geq 0. \tag{22}$$

This definition accommodates multiple contacts per finger, since each contact contributes a nonnegative closing component. Projecting Eq. (21) onto $\mathbf{e}_p$ and eliminating the normal force magnitude using Eq. (22) yields the maximum pulling contribution of contact i:

$$f_{p,i} = f_{gr,i}\left(\tan\theta_i + \mu\right). \tag{23}$$

Since Eq. (23) is linear in $f_{gr,i}$, the maximum pulling force under a fixed total grasp force is obtained by optimally distributing f_{gr} among all contacts subject to per-finger actuation limits. Let $\mathcal{F}_m$ denote the set of contacts belonging to finger $m \in \{1, \dots, M\}$, where each finger may have multiple pads. For a symmetric two-finger grasp ($M = 2$) with equal actuation,

$$\sum_{i\in\mathcal{F}_1} f_{gr,i} = \frac{f_{gr}}{2}, \qquad \sum_{i\in\mathcal{F}_2} f_{gr,i} = \frac{f_{gr}}{2}. \tag{24}$$

Define the per-contact coefficient

$$c_i(\mathbf{e}_p) = \max\left(\tan\theta_i + \mu, 0\right). \tag{25}$$

Because the objective is linear, the optimal solution assigns each finger's grasp share to the contact on that finger with the largest coefficient. Let

$$c_1^\star = \max_{i\in\mathcal{F}_1} c_i, \qquad c_2^\star = \max_{i\in\mathcal{F}_2} c_i. \tag{26}$$

Then the maximum achievable pulling force is

$$f_p^{\max} = \frac{f_{gr}}{2} c_1^\star + \frac{f_{gr}}{2} c_2^\star. \tag{27}$$

For geometrically symmetric grasps where $c_1^\star = c_2^\star = c^\star$, Eq. (27) reduces to

$$f_p^{\max} = f_{gr}\, c^\star. \tag{28}$$

Eq. (27) provides a general closed-form 3D solution for the maximum pulling force. It shows that the pulling capacity depends on:

1. *Contact orientation* through $\tan\theta_i$, which captures how passive pad alignment reorients the normal relative to the pulling direction.
2. *Friction* through μ, which determines the angular aperture of the friction cone.
3. *Active contact selection*, since only contacts with positive coefficients c_i contribute to load support.

This formulation generalizes the planar result and explains how multi-contact 3D pad arrangements expand the GWS along task-relevant directions.

The above analysis is intended as a simplified geometric and force-based interpretation of the proposed contact mechanism. Its role is to support interpretation of the experimental results obtained for the tested grasping configurations, rather than to provide a general assessment across all object geometries and manipulation tasks.

2.4. Experimental setup

To evaluate the finger designs, we used a Schunk SEG-10 electric gripper with a maximum grasp force of 170 N and a 60 mm stroke length [24]. The gripper was controlled via analog input. Two JR3 six-axis force/torque sensors, each with a measurement range of up to 150 N and a resolution of 0.05 N, were mounted between the gripper fingers and base jaw to measure grasp forces. These sensors provided real-time input to the gripper's closed-loop force control system. The experimental setup is shown in Fig. 7.

The control scheme included two modes: when the fingers are not in contact with the object, a position controller was used; upon contact, control switches to a force controller. During position control testing, the force controller was deactivated two seconds after initial contact with the object, after which the position controller resumed to maintain a fixed finger position. The control loop, implemented in MATLAB Simulink on an xPC target, operated at a 500 Hz refresh rate. High-level control and test execution were managed on a separate computer using MATLAB and Python scripts, with UDP communication between components. The control system and data flow are detailed in Fig. 8.

The performance of different finger designs was assessed through systematic pull-off force testing using a controlled experimental setup. A UR5e six-axis industrial robot (5 kg payload capacity) was employed to apply vertical pulling forces, with the gripper mounted using a custom 3D-printed adapter. Test objects were attached to a JR3 force sensor mounted on a sliding carriage mechanism positioned on a linear rail, enabling passive self-alignment during gripper closure. The UR5e applied vertical displacement at a constant velocity until object slippage occurred, while the JR3 sensor measured the resulting pull-off forces. The JR3 sensors were used to compare the measured pull-off force with the theoretical pull-off force f_p, calculated in Eq. (18). Force sensors were zeroed before each test to ensure accuracy. The robot was positioned at a consistent offset from the manually

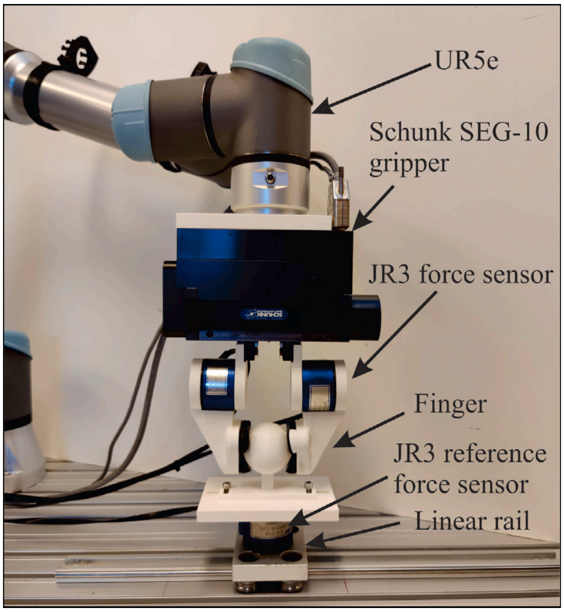

Fig. 7. Experimental setup with the UR5e robot and Schunk SEG-10 gripper.

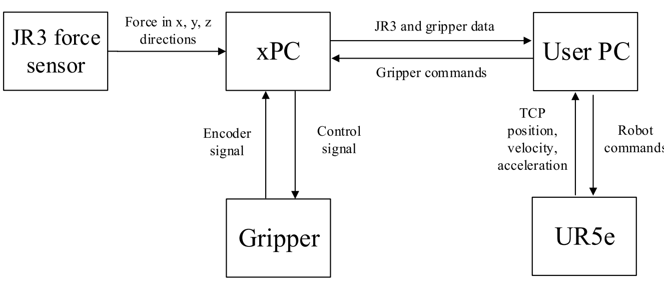

Fig. 8. Block diagram of the experimental setup, illustrating data flow and control signals among the JR3 force sensor, xPC target, gripper, UR5e robot, and user PC.

determined optimal contact point for each object-finger pair. Optimal points were determined via preliminary tests to maximize contact area. After completing 30 tests (10 grasp forces × 3 repetitions), raw data was exported for analysis. This standardized method ensured consistent conditions across finger designs.

We tested multiple finger designs (shown in Fig. 9) across grasp forces ranging from 2 N to 20 N, using a variety of test object geometries and sizes. The finger designs varied in both surface material, such as rubber and soft silicone, and structural configuration, including rigid straight fingers and adaptive fingers. In total, four combinations of these properties were evaluated, along with a baseline comparison using industry-standard Fin Ray fingers. These four configurations were selected to separate the effects of structural adaptation and the compliant surface layer: the comparison between flat and adaptive fingers isolates the contribution of the articulated pad structure, while the comparison between rubber-coated and silicone-coated fingers isolates the contribution of the compliant surface layer.

The proposed adaptive fingers (d) are characterized by several key structural parameters, summarized in Table 1. These parameters influence the fingertip's behavior: pad diameter determines contact area and achievable rotation; the distance between the pads defines the initial contact geometry and affects grasp stability; rigid PLA ensures minimal deformation and simplifies manufacturing; 2 mm silicone thickness provides a soft layer without restricting rotation; groove clearance controls joint stability while allowing smooth rotation; low groove

Table 1
Key structural parameters of the proposed adaptive fingers.

Parameter	Value
Pad diameter	20 mm
Distance between pads	30 mm
Pad material type	PLA plastic
Silicone thickness	2 mm
Groove clearance	0.1 mm
Groove friction coefficient	~ 0.2
Maximum pad rotation	25°

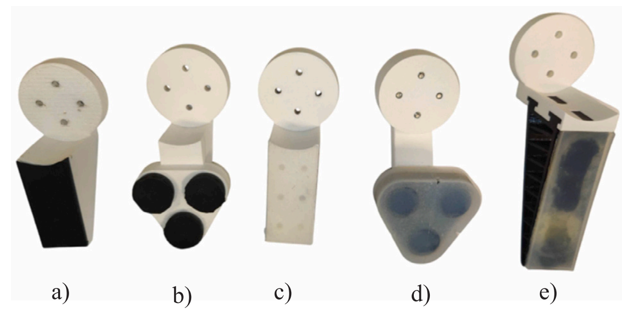

Fig. 9. Finger designs: (a) flat fingers, (b) adaptive fingers, (c) flat fingers with a soft layer, (d) adaptive fingers with a soft layer, (e) Fin Ray fingers.

friction, provided by a thin layer of silicone grease, enables passive alignment under small forces; and the maximum 25° pad rotation defines the range of morphological adaptation for object alignment.

Fingers (a) are simple rigid straight fingers coated with a hard rubber surface layer. This rubber provides increased friction during grasping but offers no damping or compliance. Fingers (b) are adaptive fingers that use the proposed pad design arranged in an equilateral triangle configuration. Each pad is covered with the same rubber material as fingers (a) and is held in place by a magnet embedded in the finger body. The magnets serve to prevent pad detachment and maintain alignment when the pads are not in contact with an object.

Fingers (c) are rigid straight fingers coated with a 3 mm layer of soft silicone. Small indentations were added to the finger surface to improve adhesion between the silicone and the rigid base. Fingers (d) are adaptive fingers fully covered in soft silicone. The silicone was poured over all three pads simultaneously, enveloping the entire upper section of the finger. This continuous layer improves durability, secures the pads in their grooves, and protects the mechanism from dust and debris. Dragon Skin 20 silicone was selected for its excellent flexibility and durability [25], making it suitable for this application. A channel in the rear section of the finger base further secures the silicone layer, preventing accidental detachment.

Fingers (e) replicate Fin Ray structures [26] and were 3D-printed using flexible TPU with a Shore hardness of 90 A. A 3 mm coating of Dragon Skin 20 silicone was also applied to the surface of the Fin Ray fingers. This enables a fair comparison with other finger designs.

Six 3D-printed PLA objects were used to test the finger prototypes, shown in Fig. 10: (a) a sphere with a 50 mm diameter, (b) a sphere with a 70 mm diameter, (c) a sphere with a 90 mm diameter, (d) a cylinder with a 70 mm diameter, (e) a cube with a 70 mm width and (f) an indented cube with the same width. All of the objects were sanded for surface smoothness and mounted on a standardized base. The chosen object geometries enable estimation of grasp performance for more complex objects.

2.5. Data analysis

Raw data were processed in MATLAB 2023a. A zero-phase, 4th-order Butterworth low-pass filter with a 5 Hz cutoff frequency was

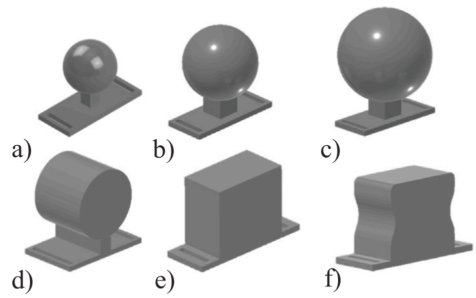

Fig. 10. All six test objects that were used during testing.

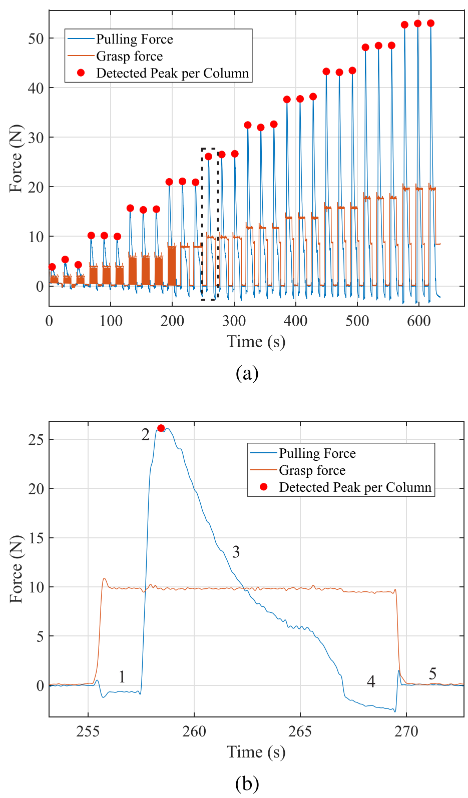

Fig. 11. (a) Raw pulling and grasp force data from pull-off tests using the proposed adaptive fingers on a sphere with a 70 mm diameter, tested across grasp forces ranging from 2 N to 20 N. (b) Detailed view of a single pull-off test at a 10 N grasp force, corresponding to the region highlighted by the dotted line in (a). Numbers from 1 to 5 represent different grasp phases.

applied using `filtfilt`. Fig. 11(a) shows filtered grasp and pulling force data. Maximum pulling forces f_p for each test were extracted using `findpeaks`, marked as red dots in Figs. 11(a) and 11(b). For grasp forces from 2 N to 20 N, the mean and standard deviation of three peak values per force were calculated. These values were plotted, with grasp force on the x-axis and pulling force on the y-axis.

Fig. 11(b) shows a single pull-off test at 10 N grasp force with the proposed adaptive fingers grasping a 70 mm diameter sphere. Pulling force (blue) and grasp force (red) are plotted. Grasp force slightly exceeds 10 N initially but stabilizes near 10 N. On the graph, we can clearly see different phases of the pulling procedure. First when the gripper comes into contact with the object it pushes the object slightly downwards which we can see on the graph by the negative pulling force (phase 1 in Fig. 11(b)). At this stage the robot is still stationary. When the robot starts to move upwards the pulling force quickly increases to its maximum (phase 2 in Fig. 11(b)). The maximum achieved force is represented by a red dot. The force then starts to slowly drop as the grasped object slips from its optimal grasping position (phase 3 in Fig. 11(b)). When the robot reaches its upper limit it stops (represented by phase 4 in Fig. 11(b)). After the robot stops the gripper opens. When the gripper opens the pulling force drops to 0 N (phase 5 in Fig. 11(b)). Then the robot moves to the starting position and the experiment repeats. The whole procedure takes 15 s to complete. Different finger types and object combinations produce different responses.

3. Results

3.1. Gripper force and position control test

The gripper can operate in two modes: force control and position control. During force control gripper reaches force closure, it maintains constant grasp force by adjusting finger positions based on force sensor feedback, keeping contact forces within the friction cone, defined by μ in Eq. (18), to prevent slippage. This mode suits fragile objects, preventing damage by regulating f_{gr}. During position control gripper reaches form closure, the fingers move to a predefined position, using geometric constraints to stabilize the object during high-force tasks. In contrast, force closure is more relevant for dynamic manipulation, as it adapts to external disturbances without relying solely on geometric constraints. To test these two control modes we conducted pull-off force tests on a deformable spherical object with 70 mm radius using the proposed adaptive finger design. A deformable object was selected to prevent excessive forces, since rigid form closure would exceed the system's capacity. This also served as a safety measure, allowing the object to deform without equipment damage. The tests were conducted using grasp forces ranging from 0.5 N to 6 N, in increments of 0.5 N.

We tested both modes with the proposed adaptive finger design. In force control mode, the gripper continuously adjusts to maintain the desired grasp force, as indicated by the steady blue line in Fig. 12(a). If the grasp force increases during the pull-off force test, the fingers move apart to avoid exceeding the set force. This method is ideal for handling fragile objects, where precise force regulation is critical [16].

In position control, the fingers move to grasp an object until a predetermined force is reached, at which point they stop, achieving form closure preventing slippage via geometric constraints. This yields higher pulling forces, as shown in Figs. 12(b) and 13. Fig. 12(a) illustrates how the grasp force exceeds the set value during the pull-off test in position control, a result of geometric locking. The results, depicted in Figs. 12(b) and 13, show that the maximum pulling force under position control is approximately 2-3 times higher than under force control. This ratio would be even higher if the grasped object were not deformable. The results demonstrate that proposed adaptive fingers are capable of reliably achieving both form and force closure grasps.

3.2. Pull-off force test

To evaluate how the proposed adaptive fingers compare to other designs described in Section 2.1, we conducted pull-off force tests on six objects with varied shapes and sizes. The results are shown in Fig. 14. All tests were performed using force control. The horizontal axis represents grasp force (2 N to 20 N, 10 different values with increments of 2 N), and the vertical axis represents pulling force, measured by a base-mounted force sensor. Each point averages three maximum pulling forces from repeated tests, with standard deviations indicated.

Most results exhibit an approximately linear relationship between grasp force and maximum pulling force, which is in broad agreement with the trend predicted by Eq. (18). A notable exception is the Fin Ray finger design, which shows near-linear behavior at low grasp forces but a weaker increase in pulling force at higher grasp forces, typically reaching a maximum at grasp forces of 14–16 N. The graphs show small standard deviations (< 5%) for most data points.

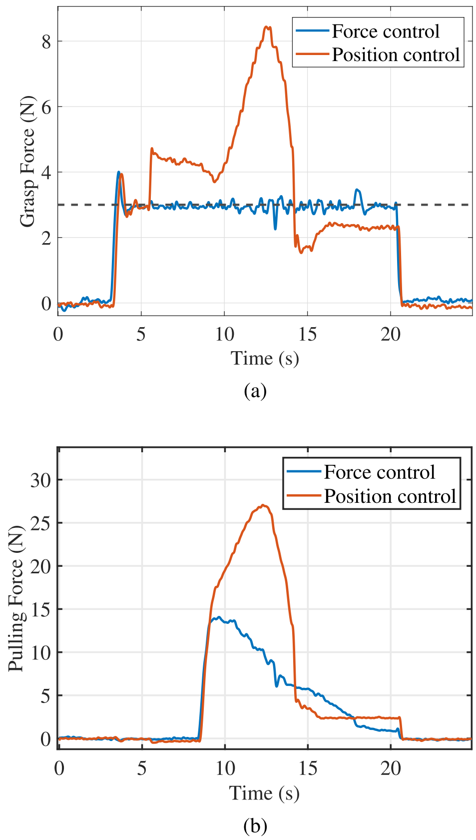

Fig. 12. Comparison of grasp force (a) and pulling force (b) for the proposed adaptive fingers under force (blue line) and position (red line) control during a pull-off force test while grasping a 70 mm soft ball at a set grasp force of 3 N.

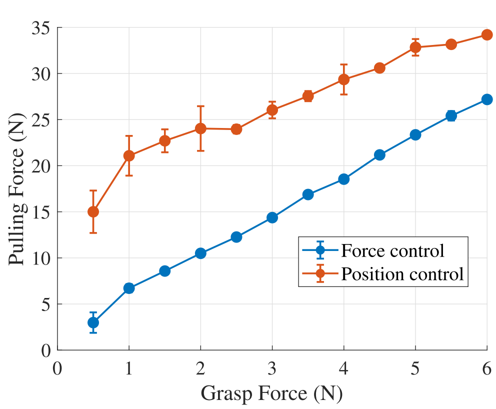

Fig. 13. Maximum pulling force of adaptive fingers with a silicone layer while grasping a soft ball with a 70 mm diameter relative to grasp force. The blue line represents force control, and the red line represents position control.

To provide a clearer comparison, we calculated a pulling performance index for each finger type. The index is obtained by dividing the pulling force by the grasp force for each data point, then averaging these values. Simultaneously we also calculated the standard deviation. The results are presented in Fig. 15. The average pulling performance index I quantifies the efficiency of gripper designs by measuring the ratio of pulling force to grasp force across test conditions. It is defined as:

$$I = \frac{1}{N} \sum_{i=1}^{N} \frac{f_{p,i}}{f_{gr,i}}, \tag{29}$$

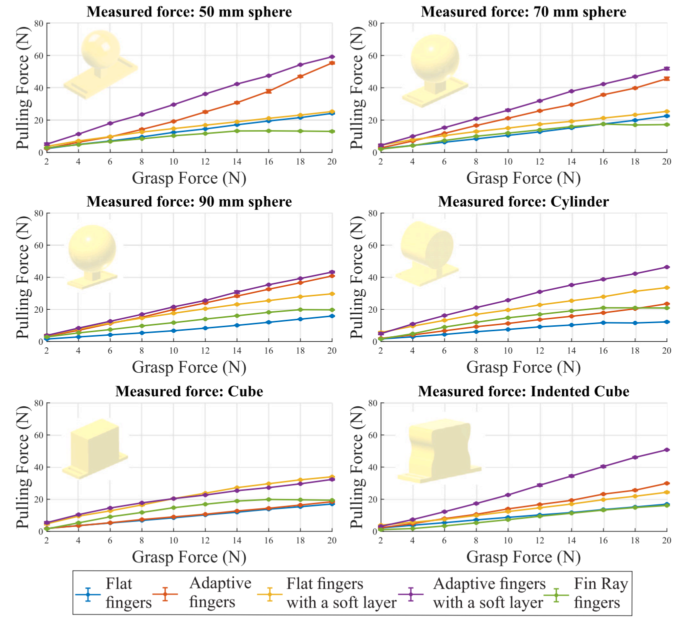

Fig. 14. Pull-off force test results for six different test objects. The horizontal axis represents the grasp force exerted by the gripper, while the vertical axis represents the pulling force.

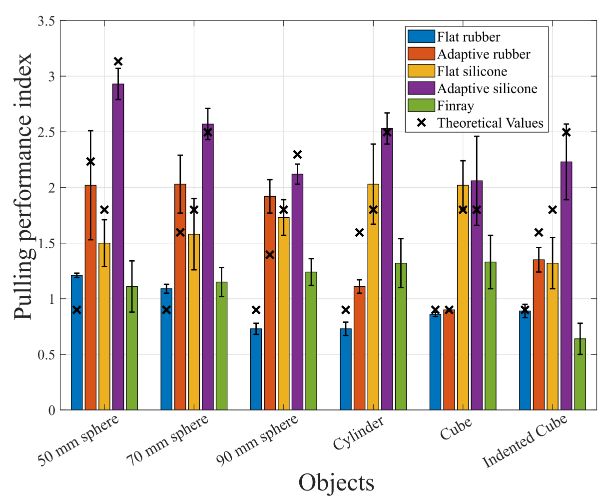

Fig. 15. Grouped bar plot of pulling performance indexes with error bars. The horizontal axis represents different test objects, while the vertical axis represents the pulling performance index. For all finger types (except the Fin Ray fingers) the corresponding theoretical values predicted by the analytical model are also indicated by × symbols.

where $f_{p,i}$ is the pulling force, $f_{gr,i}$ is the corresponding grasp force for the ith test, and N is the number of grasp force levels.

The bar plot (Fig. 15) demonstrates that the proposed adaptive finger design achieved the best overall performance across all tested objects. The most significant advantages were observed for the three spheres of different radii and the cylinder. While pulling the cube, the performance of the adaptive fingers with a silicone layer matched that of flat fingers with a silicone layer, which is consistent with the reduced geometric benefit of articulated pads on flat contact surfaces. The Fin Ray fingers, which are the current industry standard for soft grasping, consistently underperformed compared to the proposed adaptive finger design across all tested objects. Fin Ray fingers plateau due to structural deformation, limiting maximum pulling force f_p.

The pulling performance index quantifies how effectively each finger design converts grasp force into pull-off force, with higher values indicating enhanced grasp efficiency. Among all tested configurations, the proposed adaptive fingers with a soft silicone layer achieved the highest average index of 2.4, significantly outperforming the other designs. Adaptive fingers with rubber pads followed with an average index of 1.6, while flat silicone-coated fingers achieved 1.7. In contrast, flat fingers with a rubber surface reached a lower average index of 0.9. The widely used Fin Ray fingers achieved an index of 1.1, trailing behind both designs with articulated hemispherical pads. These comparisons also help distinguish the contribution of the main design choices. The improvement from flat rubber fingers to adaptive rubber fingers reflects the contribution of the articulated pad structure, particularly for curved geometries where passive pad reorientation improves load sharing. The improvement from flat rubber fingers to flat fingers with a silicone layer reflects the contribution of the compliant surface layer through increased effective contact area and friction. The adaptive fingers with a silicone layer combine both effects and therefore achieve the highest overall pulling performance index, indicating that the best performance arises from the combined effect rather than from either design feature alone.

Fig. 15 also compares the measured pulling performance index with the theoretical values predicted by the analytical model, marked by × symbols. Theoretical values are not shown for the Fin Ray fingers because the analytical model was developed specifically for the proposed adaptive finger concept, while the Fin Ray fingers were included only as a reference design. Both the theoretical and experimental results show that fingers with adaptive pads achieve higher pulling performance than flat fingers of the same surface type. Likewise, fingers with a silicone layer consistently outperform the corresponding fingers coated with rubber, indicating the additional contribution of compliant, high-friction surface contact. For adaptive fingers with a silicone layer, both theory and experiments show that larger pad angles are associated with higher pulling performance. In the tests with spherical objects, smaller sphere radii result in larger pad angles. For adaptive fingers with rubber pads, the same tendency is less pronounced experimentally: the effect of pad angle is already evident for the larger-radius sphere and does not increase substantially with further increase in pad angle. The main deviations between theory and experiment therefore concern the magnitude of the improvement, rather than the overall direction of the effect.

For the flat finger designs, the effective friction coefficient μ can be estimated from the relationship between the measured pulling force and the applied grasp force when grasping a cube (Fig. 14). Using this approach, we obtained representative values of $\mu = 0.83$ for flat (rubber-coated) fingers and $\mu = 2.5$ for flat fingers with a soft silicone layer. These values illustrate how surface material directly influences grasp stability, with higher friction coefficients enabling greater pulling forces. It should be noted that μ is affected by factors such as surface roughness, material properties, and environmental conditions.

3.3. Soft object deformation test

To assess the influence of different finger types on the structural deformation of a soft object, deformation measurements were conducted on a 70 mm soft foam ball. Small linear motion potentiometers were embedded within the material of the test object to measure local deformations. The movable rods of the potentiometers were mechanically coupled to the surface of the sphere, allowing direct measurement of surface deformation during grasping.

A total of four potentiometers were used. One potentiometer was positioned at the center of the sphere and aligned with the center of the contact area between the object and the finger. The remaining three potentiometers were placed at a radial distance of 12 mm from the central sensor and distributed uniformly at angular intervals of 120°. The analog output signals from all potentiometers were acquired using an A/D converter. These measurements enabled accurate determination of the displacement of each sensing point during the grasping process.

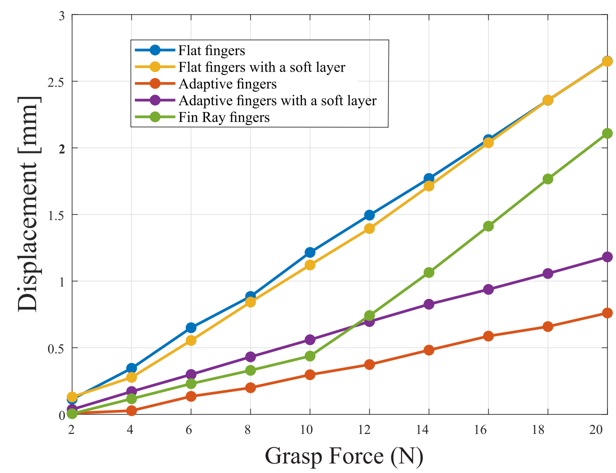

Fig. 16. Soft object deformation test results for different finger types. The horizontal axis represents the grasp force exerted by the gripper, while the vertical axis represents the maximum displacement of the sensors integrated in the soft sphere.

Five repetitions were performed at grasp force levels ranging from 2 N to 20 N in 2 N increments. For each grasp force level, the measurements from five repetitions were averaged. The sensor exhibiting the maximum deformation (typically the sensor positioned at the center of the object) was then selected, and its averaged values were plotted (Fig. 16). This approach focuses on worst-case local deformation, which is most relevant for assessing potential object damage.

4. Discussion

The proposed adaptive gripper finger design combines articulated hemispherical pads and a compliant silicone layer to address the practical trade-off between shape accommodation and load-bearing capability. Compared with hybrid designs that rely primarily on compliance of the contact surface [27,28], the presented design uses passively reorienting rigid pads to redistribute contact forces while retaining a compliant outer layer. This rigid yet adaptive structure balances the adaptability of soft grippers, which conform well to shapes but lack strength, with the force capacity of rigid grippers.

This enables two key mechanisms:

1. **Load sharing:** The pads align with the object's shape, creating multiple distributed contact points to prevent localized stress peaks. This is achieved through low friction grooves that allow the pads to reconfigure, ensuring uniform pressure distribution.
2. **Structural rigidity:** Rigid pads preserve the finger's structural integrity under high manipulation forces, avoiding the deformation common in soft grippers.

The pad and groove geometry (Section 2.1) was chosen to ensure stable and predictable passive rotation under load. While sub-hemispherical and super-hemispherical geometries allow pad rotation, they are more sensitive to contact location and object curvature. In contrast, hemispherical pads provide consistent contact normal alignment for the representative object geometries considered here, making them a suitable choice for the tested grasping scenarios. More generally, robotic fingers are typically designed for a particular application and object class rather than for arbitrary object geometries. The present finger embodiment was therefore developed for the representative objects considered in this study, which provide sufficiently extended contact regions for simultaneous multi-pad engagement. For smaller or more slender objects, the same design principle could be adapted by changing finger size, pad size, pad number, or pad arrangement to better match the target object geometry and task requirements.

The force-closure analysis illustrates how passive pad reorientation modifies friction-cone alignment, resulting in a larger modeled grasp wrench space than in the flat parallel-finger configuration (Fig. 5). The resulting relationship between pulling force (f_p), grasp force (f_{gr}), and contact angle (θ) is consistent with the experimentally observed trends in pull-off performance (Fig. 14). These analytical results should be interpreted as mechanism-level explanations under simplified contact assumptions and within the scope of the tested grasping conditions in this study, specifically pull-off force performance, force- versus position-controlled grasping, and soft-object deformation for the representative object set considered here.

Pull-off force testing serves as a useful basis for comparing the relative performance of different robotic gripper finger designs [17,18]. Fig. 14 presents the maximum pull-off forces measured across grasp forces ranging from 2 N to 20 N. As shown in Fig. 14, the proposed adaptive fingers consistently achieve higher pull-off forces than the reference designs across the tested grasp force range, with the advantage becoming more pronounced at higher grasp forces (above 16 N). At these loads, the fully soft Fin Ray fingers exhibit substantial structural deformation that limits effective force transmission, whereas the rigid articulated pads of the proposed design preserve contact geometry and load-bearing capability. As a result, the adaptive fingers attain a substantially higher pulling performance index than the Fin Ray design. These trends are consistent with prior studies highlighting the influence of object geometry on grasp performance [17,18], although differences in experimental conditions and material properties prevent direct comparison of absolute force values. The comparative results indicate that the articulated pads primarily contribute geometric adaptation and load sharing, whereas the silicone layer primarily contributes increased effective contact area, higher friction, and reduced localized deformation of the object. The best overall performance is obtained when both mechanisms are combined.

A direct comparison between the analytical pulling-force model and the experimental pull-off results shows good agreement in the main qualitative trends. In both theory and experiment, fingers with adaptive pads outperform flat fingers of the same surface type, and fingers with a silicone layer outperform the corresponding rubber-coated fingers. For adaptive fingers with a silicone layer, larger pad angles are associated with higher pulling performance in both theory and experiment. For adaptive fingers with rubber pads, the same tendency is less pronounced experimentally, although both theory and experiment still show an advantage over flat rubber fingers. Quantitatively, deviations remain between theoretical and measured values, with an average error of approximately 20%. The largest deviations occur in comparisons between adaptive fingers with rubber pads and flat fingers with a silicone layer, where the simplified model does not fully capture the combined effects of pad rotation, friction under the pads, and compliant surface contact. This is expected because the analytical model is based on a simplified hard-finger, Coulomb-friction contact description, whereas the experiments involve additional effects such as compliant deformation, non-uniform load sharing, friction in the pad grooves, and uncertainty in the effective friction coefficient. More accurate prediction would require compliant or soft-finger contact models with finite contact area, geometry-dependent friction constraints, and stiffness-dependent behavior, which would substantially increase analytical and experimental complexity [20,29,30]. The analytical model should therefore be interpreted as an analytical description of the dominant grasping mechanism and the main experimental trends, rather than as an exact quantitative predictor of pull-off force.

When grasping soft objects that are susceptible to damage, the most relevant indicator of potential damage is the maximum surface deformation. For this reason, we designed a dedicated measurement device consisting of a soft 70 mm foam sphere instrumented with four linear motion potentiometers, enabling precise measurement of object deformation during grasping. The results of this test are shown in Fig. 16. The measurements demonstrate that the proposed adaptive finger design produces significantly smaller deformations of the soft object compared to flat fingers, with approximately two times lower maximum deformation. Instead of the soft object deforming, the pads on the proposed fingers rotate and the silicone layer deforms since it is made of a softer material than the grasped object.

During repeated pull-off force tests we observed wear and tear of different fingers. The silicone layer of the adaptive fingers showed no visible wear when grasping smooth, rounded objects, whereas localized damage occurred when handling objects with sharp edges, particularly the rectangular geometry. Early prototypes using softer silicone degraded rapidly under these conditions, motivating the use of Dragon Skin 20 silicone with a higher durometer, which significantly improved resistance to tearing and abrasion. For applications where durability is prioritized over compliant contact, such as industrial handling of sharp-edged objects, the silicone layer can be replaced with harder coatings such as rubber or polyurethane.

The soft layer in the proposed design is modular and can be easily detached and replaced without tools, enabling maintenance or customization based on task requirements. The soft layer was fabricated via silicone molding, using specially designed molds. The 3D-printed PLA pads were inserted into the molds prior to pouring the silicone, and specially designed grooves on the pad surfaces ensure strong adhesion between the silicone and the pads.

The proposed adaptive finger design allows rapid modification of key parameters to accommodate different application requirements. Surface compliance can be tuned by selecting alternative contact-layer materials, ranging from silicone compounds with varying Shore hardness to rubberized or rigid coatings for applications where soft contact is not required. The design further allows variation in the number, size, and spatial arrangement of the rotating pads, as well as adaptation of the finger base geometry to specific object profiles, for example by introducing curvature to achieve noncoplanar pad placement and improved shape conformity.

From an integration perspective, the adaptive finger design is mechanically compatible with a wide range of robotic grippers and performs effectively under both position-controlled and force-controlled grasping modes (Section 3.1). This versatility enables integration with most commercially available industrial grippers, including systems without active force feedback. For applications involving soft or fragile objects, pairing the fingers with a gripper capable of precise force control is recommended to reduce the risk of damage. The design readily extends to multi-finger configurations, such as three-finger grippers, increasing the contact area and improving grasp stability. Its modular structure and simple fabrication process, based on 3D printing and silicone molding, support rapid prototyping and iterative design refinement. For applications requiring higher stiffness or increased grasp forces, the pads and housing can be manufactured from aluminum or other rigid materials, preserving the overall geometry while enhancing structural robustness.

The current experimental setup employs a JR3 six-axis force/ torque sensor to measure interaction forces during grasping. Although this sensor provides high measurement accuracy, its size and cost make it impractical for deployment in real-world robotic systems. Future work will therefore focus on integrating compact force sensing directly into the finger design. One approach is to embed multiple force-sensing resistors (FSRs) beneath the silicone layer to obtain localized contact information, enabling slip detection and coarse force estimation. For higher-accuracy force measurement without increasing the finger footprint, a custom load cell can be integrated at the gripper base. Looking further ahead, the design could accommodate the integration of miniature cameras beneath the transparent silicone layer (similar to [31]). These vision-based tactile sensors would allow for real-time observation of contact deformation patterns, which could be processed using AI algorithms to extract detailed surface interaction data.

5. Conclusion

This study presented an adaptive gripper finger design that integrates a compliant silicone layer with passively aligning articulated pads to address the challenge of achieving both shape adaptability and strong force transmission in robotic grasping. The mechanical configuration enables simultaneous shape conformity and structural integrity under load, with the silicone layer improving friction and contact area.

The proposed design is compatible with scalable fabrication methods, including 3D printing and silicone molding, enabling easy adaptation to different application-specific finger configurations. Experimental validation consisted of systematic pull-off force tests on six object geometries using five different finger designs, complemented by deformation experiments on a soft spherical object. The results demonstrate that the proposed adaptive fingers achieved both the highest pulling performance index (2.4) and the lowest deformation of a soft object, outperforming conventional flat and Fin Ray finger designs.

The analysis demonstrated that the design maintains effective force or form closure and shape conformity for the tested object geometries and experimental conditions, particularly under both position-controlled (form closure) and force-controlled (force closure) grasp modes. Force closure and pulling force models showed a linear grasp-to-pull force relationship. These findings confirm the suitability of the design for tested grasping scenarios requiring both delicate and stable grasping.

Potential application areas include robotic handling tasks that require both compliant contact and sufficient load-bearing capability. Examples include agricultural handling of delicate produce and laboratory automation involving fragile containers or tools. These application areas remain prospective, and their suitability should be evaluated in future task-specific studies.

The results indicate that the proposed finger architecture is a promising design option for grasping tasks where both load-bearing capability and compliant contact are desirable. The present study demonstrates these advantages for the tested object set and experimental conditions. The contribution of this work lies primarily in the mechanical design and experimental validation of the finger architecture, while the analytical models are used to interpret the observed grasping behavior. Future work will evaluate performance on a broader range of object geometries, including slender and small-diameter objects, and in real-world handling tasks.

CRediT authorship contribution statement

Tilen Klemenčič: Writing – review & editing, Writing – original draft, Visualization, Validation, Software, Methodology, Investigation, Formal analysis, Data curation, Conceptualization. **Marko Munih:** Writing – review & editing, Supervision, Project administration, Funding acquisition. **Matjaž Mihelj:** Writing – review & editing, Project administration, Methodology, Investigation, Conceptualization. **Janez Podobnik:** Writing – review & editing, Writing – original draft, Validation, Software, Project administration, Methodology, Investigation, Formal analysis, Data curation, Conceptualization.

Declaration of competing interest

The authors declare that they have no known competing financial interests or personal relationships that could have appeared to influence the work reported in this paper.

Acknowledgments

This work was funded by the DIGITOP project (Grant No. TN-06-0106), the project "Versatile AI-Driven Robotic System for Plant and Produce Management" (Grant No. L2-60143), and the Slovenian Research and Innovation Agency under programme P2-0228.

Appendix A. Supplementary data

Supplementary material related to this article can be found online at https://doi.org/10.1016/j.mechatronics.2026.103534.

Data availability

Data will be made available on request.

References

[1] Birglen L, Schlicht T. A statistical review of industrial robotic grippers. Robot Comput-Integr Manuf 2018;49:88–97.
[2] Liu Y, Hou J, Li C, Wang X. Intelligent soft robotic grippers for agricultural and food product handling: A brief review with a focus on design and control. Adv Intell Syst 2023;5(12):2300233.
[3] Bicchi A. Hands for dexterous manipulation and robust grasping: a difficult road toward simplicity. IEEE Trans Robot Autom 2000;16(6):652–62.
[4] Billard A, Kragic D. Trends and challenges in robot manipulation. Science 2019;364(6446):eaat8414. http://dx.doi.org/10.1126/science.aat8414.
[5] Hernandez J, Sunny MSH, Sanjuan J, Rulik I, Zarif MII, Ahamed SI, Ahmed HU. Current designs of robotic arm grippers: A comprehensive systematic review. Robotics 2023;12(1). http://dx.doi.org/10.3390/robotics12010005.
[6] AboZaid YA, Aboelrayat MT, Fahim IS, Radwan AG. Soft robotic grippers: A review on technologies, materials, and applications. Sensors Actuators A: Phys 2024;372:115380.
[7] Terrile S, Argüelles M, Barrientos A. Comparison of different technologies for soft robotics grippers. Sensors 2021;21(9). http://dx.doi.org/10.3390/s21093253.
[8] Elgeneidy K, Lohse N, Jackson M. Bending angle prediction and control of soft pneumatic actuators with embedded flex sensors - a data-driven approach. Mechatronics 2018;50:234–47. http://dx.doi.org/10.1016/j.mechatronics.2017.10.005.
[9] Maggi M, Mantriota G, Reina G. Combining underactuation with vacuum grasping for improved robotic grippers. Mechatronics 2024;102:103211. http://dx.doi.org/10.1016/j.mechatronics.2024.103211.
[10] Hamon P, Michel L, Plestan F, Chablat D. Model-free based control of a gripper actuated by pneumatic muscles. Mechatronics 2023;95:103053. http://dx.doi.org/10.1016/j.mechatronics.2023.103053.
[11] Kaur M, Kim WS. Toward a smart compliant robotic gripper equipped with 3d-designed cellular fingers. Adv Intell Syst 2019;1(3):1900019. http://dx.doi.org/10.1002/aisy.201900019.
[12] Hughes J, Culha U, Giardina F, Guenther F, Rosendo A, Iida F. Soft manipulators and grippers: A review. Front Robot AI 2016;3.
[13] Sun Y, Liu Y, Pancheri F, Lueth TC. LARG: A lightweight robotic gripper with 3-D topology optimized adaptive fingers. IEEE/ASME Trans Mechatronics 2022;27(4):2026–34. http://dx.doi.org/10.1109/TMECH.2022.3170800.
[14] Srinivas GL, Alshawabkeh A, Brandstötter M. Design and development of fin-ray finger using topology optimization with multiple load cases. In: Proc. International Conference on Cognitive Robotics and Intelligent Systems (ICC - ROBINS). 2024, p. 1–7. http://dx.doi.org/10.1109/ICC-ROBINS60238.2024.10534011.
[15] Chang C-M, Gerez L, Elangovan N, Zisimatos A, Liarokapis M. On alternative uses of structural compliance for the development of adaptive robot grippers and hands. Front Neurorobotics 2019;13. http://dx.doi.org/10.3389/fnbot.2019.00091.
[16] Li Z, Li P, Yang H, Wang Y. Stability tests of two-finger tomato grasping for harvesting robots. Biosyst Eng 2013;116(2):163–70.
[17] Hao Y, Gong Z, Xie Z, Guan S, Yang X, Ren Z, Wang T, Wen L. Universal soft pneumatic robotic gripper with variable effective length. In: 2016 35th Chinese control conference. CCC, 2016, p. 6109–14. http://dx.doi.org/10.1109/ChiCC.2016.7554316.
[18] Białek M, Rybarczyk D. A comparative study of different fingertips on the object pulling forces in robotic gripper jaws. Appl Sci 2023;13(3). http://dx.doi.org/10.3390/app13031247.
[19] Choi YT, Hartzell CM, Leps T, Wereley NM. Gripping characteristics of an electromagnetically activated magnetorheological fluid-based gripper. AIP Adv 2017;8(5):056701. http://dx.doi.org/10.1063/1.5006094.
[20] Prattichizzo D, Trinkle JC. Grasping. In: Springer handbook of robotics. Berlin, Heidelberg: Springer; 2008, p. 671–700. http://dx.doi.org/10.1007/978-3-540-30301-5_29.
[21] Ferrari C, Canny J. Planning optimal grasps. In: Proceedings 1992 IEEE international conference on robotics and automation. vol.3, 1992, p. 2290–5. http://dx.doi.org/10.1109/ROBOT.1992.219918.
[22] Ding D, Liu Y-H, Zhang J, Knoll A. Computation of fingertip positions for a form-closure grasp. Proceedings 2001 iCRA. IEEE international conference on robotics and automation, Vol. 3, 2001, p. 2217–22. http://dx.doi.org/10.1109/ROBOT.2001.932952, vol.3.

[23] Pollard NS. Parallel methods for synthesizing whole-hand grasps from generalized prototypes. (Ph.D. dissertation), Cambridge, MA: Massachusetts Institute of Technology; 1994, Available: https://dspace.mit.edu/handle/1721.1/7055.

[24] Fritz Schunk GmbH, High Technology Workholding. Description and operating instructions: servo gripper seg-10. 1988, Schunk GmbH, Lauffen/Neckar, Germany, Document No. 03/00050/E..

[25] Smooth-On, Inc. Dragon skin™ 20 product information. 2025, https://www.smooth-on.com/products/dragon-skin-20/.

[26] Brown AS. Gripper like a hand. Mech Engineering-CIME 2009;131(9):22–3.

[27] Culha U, Hughes J, Rosendo A, Giardina F, Iida F. Design principles for soft-rigid hybrid manipulators. In: Soft robotics: trends Applications and Challenges. vol. 17, Springer International Publishing; 2017, p. 87–94.

[28] Goshtasbi A, Grignaffini L, Sadeghi A. Bio-inspired 3D printing approach for bonding soft and rigid materials through underextrusion. Sci Rep 2025;15.

[29] Bicchi A, Kumar V. Robotic grasping and contact: A review. In: Proceedings 2000 iCRA. millennium conference. IEEE international conference on robotics and automation. symposia proceedings, Vol. 1, 2000, p. 348–53. http://dx.doi.org/10.1109/ROBOT.2000.844081.

[30] Ciocarlie MT, Lackner C, Allen PK. Soft finger model with adaptive contact geometry for grasping and manipulation tasks. In: Second joint euroHaptics conference and symposium on haptic interfaces for virtual environment and teleoperator systems. WHC 2007, 2007, p. 219–24. http://dx.doi.org/10.1109/WHC.2007.103.

[31] Yuan W, Dong S, Adelson EH. GelSight: High-Resolution Robot Tactile Sensors for Estimating Geometry and Force. Sensors 2017;17(12). http://dx.doi.org/10.3390/s17122762.

Tilen Klemenčič received the B.Sc. and M.Sc degrees in electrical engineering from the University of Ljubljana, Ljubljana, Slovenia, in 2020 and 2024, respectively.

He is currently a Researcher with the University of Ljubljana. His current research interests include robotic grippers, robotic gripper finger design, soft grippers.

Marko Munih received the Ph.D. degree in electrical engineering from the University of Ljubljana (UL), Ljubljana, Slovenia.

From 2004 to 2006, he was the Head of the Department for Measurements and Process Control, Faculty of Electrical Engineering, UL, where he is currently a Full Professor and the Head of the Laboratory of Robotics.

Matjaž Mihelj received the B.Sc., M.Sc., and Ph.D. degrees in electrical engineering from the University of Ljubljana, Ljubljana, Slovenia, in 1996, 1999, and 2002, respectively.

Since 2014, he has been a Full Professor with the Faculty of Electrical Engineering, University of Ljubljana.

Janez Podobnik received the B.Sc. and Ph.D. degrees in electrical engineering from the University of Ljubljana, Ljubljana, Slovenia, in 2004 and 2009, respectively.

He is currently an Assistant Professor with the University of Ljubljana. His current research interests include haptic interfaces, real-time control of robots for virtual-reality-supported rehabilitation, and sensory fusion techniques.